

See discussions, stats, and author profiles for this publication at: <https://www.researchgate.net/publication/6849897>

Crystal Structure of α -Amino- β -carboxymuconate- ϵ -semialdehyde Decarboxylase: Insight into the Active Site and Catalytic Mechanism of a Novel Decarboxylation Reaction †, ‡

ARTICLE in BIOCHEMISTRY · OCTOBER 2006

Impact Factor: 3.02 · DOI: 10.1021/bi060903q · Source: PubMed

CITATIONS

30

READS

50

6 AUTHORS, INCLUDING:



Aimin Liu

Georgia State University

79 PUBLICATIONS 1,269 CITATIONS

SEE PROFILE



Hong Zhang

University of Texas Southwestern Medical Ce...

34 PUBLICATIONS 1,025 CITATIONS

SEE PROFILE

Crystal Structure of α -Amino- β -carboxymuconate- ϵ -semialdehyde Decarboxylase: Insight into the Active Site and Catalytic Mechanism of a Novel Decarboxylation Reaction^{†,‡}

Dariusz Martynowski,[§] Yvonne Eyobo,[§] Tingfeng Li,^{||} Kun Yang,[§] Aimin Liu,^{*,||} and Hong Zhang^{*,§}

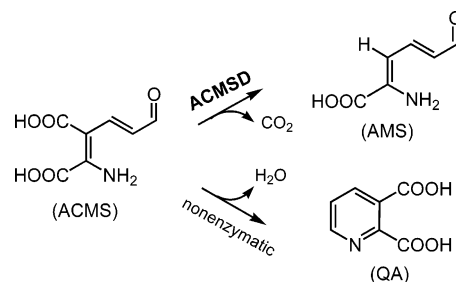
Department of Biochemistry, University of Texas Southwestern Medical Center, Dallas, Texas 75390-8816, and
Department of Chemistry, University of Mississippi Medical Center, Jackson, Mississippi 39216-4505

Received May 5, 2006; Revised Manuscript Received June 22, 2006

ABSTRACT: α -Amino- β -carboxymuconate- ϵ -semialdehyde decarboxylase (ACMSD) is a widespread enzyme found in many bacterial species and all currently sequenced eukaryotic organisms. It occupies a key position at the branching point of two metabolic pathways: the tryptophan to quinolinate pathway and the bacterial 2-nitrobenzoic acid degradation pathway. The activity of ACMSD determines whether the metabolites in both pathways are converted to quinolinic acid for NAD biosynthesis or to acetyl-CoA for the citric acid cycle. Here we report the first high-resolution crystal structure of ACMSD from *Pseudomonas fluorescens* which validates our previous predictions that this enzyme is a member of the metal-dependent amidohydrolase superfamily of the $(\beta/\alpha)_8$ TIM barrel fold. The structure of the enzyme in its native form, determined at 1.65 Å resolution, reveals the precise spatial arrangement of the active site metal center and identifies a potential substrate-binding pocket. The identity of the native active site metal was determined to be Zn. Also determined was the structure of the enzyme complexed with cobalt at 2.50 Å resolution. The hydrogen bonding network around the metal center suggests that Arg51 and His228 may play important roles in catalysis. The metal center configuration of PfACMSD is very similar to that of Zn-dependent adenosine deaminase and Fe-dependent cytosine deaminase, suggesting that ACMSD may share certain similarities in its catalytic mechanism with these enzymes. These data enable us to propose possible catalytic mechanisms for ACMSD which appear to be unprecedented among all currently characterized decarboxylases.

α -Amino- β -carboxymuconate- ϵ -semialdehyde (ACMS)¹ is an important intermediate in two metabolic pathways: (1) the tryptophan to quinolinate pathway in eukaryotes and a

number of bacteria (1, 2) and (2) the newly discovered 2-nitrobenzoic acid biodegradation by certain microorganisms (3, 4). ACMS is the end product of the five-step tryptophan to quinolinate pathway. It then undergoes a spontaneous transformation to form quinolinic acid (QA), the universal precursor for the de novo biosynthesis of NAD (1, 5). Alternatively, instead of being converted to QA and entering NAD biosynthesis, ACMS can be decarboxylated to give 2-aminomuconate semialdehyde (AMS) in a reaction catalyzed by enzyme ACMS decarboxylase (ACMSD) (6–8) (Scheme 1). AMS is then converted to acetyl-CoA through a series of transformations and eventually enters the citric acid cycle for complete oxidation and energy production. Scheme 1: ACMSD-Catalyzed Reaction



[†] This work was supported by NIH Grant GM65243 (to H.Z.) and Welch Foundation Grant I-1505. A.L. acknowledges the ORAU Faculty Enhancement Award and the partial support from a subaward of NIH Grant GM69618. Use of the Argonne National Laboratory Structure Biology Center beamline at Advanced Photon Source was supported by the U.S. Department of Energy, Office of Biological and Environmental Research, under Contract W-31-109-ENG-38.

[‡] The coordinates and structure factors for PfACMSD have been deposited in the Protein Data Bank (entries 2HBV and 2HBX for the native Zn enzyme and Co-reconstituted enzyme, respectively).

* To whom correspondence should be addressed. H.Z.: phone, (214) 645-6372; fax, (214) 645-5948; e-mail, zhang@chop.swmed.edu. A.L.: phone, (601) 984-1872; fax, (601) 984-1501; e-mail, aliu@biochem.umsmed.edu.

[§] University of Texas Southwestern Medical Center.

^{||} University of Mississippi Medical Center.

¹ Abbreviations: ACMS, α -amino- β -carboxymuconate- ϵ -semialdehyde; ACMSD, α -amino- β -carboxymuconate- ϵ -semialdehyde decarboxylase; PfACMSD, ACMSD from *Pseudomonas fluorescens*; AMS, 2-aminomuconate-6-semialdehyde; TIM, triosephosphate isomerase; EPR, electron paramagnetic resonance spectroscopy; IPTG, isopropyl β -D-thiogalactopyranoside; NAD, nicotinamide adenine dinucleotide; QA, quinolinic acid; ADA, adenosine deaminase; CDA, cytosine deaminase; rmsd, root-mean-square deviation.

Thus, ACMSD occupies a key position at the branching point of two metabolic pathways and controls the final fate of the metabolites in both pathways.

QA is not only the universal precursor for the de novo synthesis of NAD but also a potent endogenous neurotoxin via hyperstimulation of glutamate receptors that are sensitive to *N*-methyl D-aspartate (NMDA) and associated with a wide range of neurodegenerative disorders such as epilepsy, Alzheimer's disease, and Huntington's disease (9–11). Elevated levels of QA have been observed in body fluids of patients diagnosed with these disorders (9, 10, 12). Since ACMSD can be diverted to a benign metabolite AMS by ACMSD, activation of ACMSD may direct the metabolic flux to the citric acid cycle and thus prevent the progression of these diseases.

ACMSD is widely distributed in both bacteria and eukaryotic organisms, including humans. The enzyme was discovered five decades ago (13, 14). Only recently has its catalytic cofactor, a mononuclear transition metal center, been uncovered from the *Pseudomonas fluorescens* enzyme (*Pf*ACMSD) (15, 16). Since both bacterial and human ACMSD proteins share a significant degree (40% identity) of sequence similarity, they presumably also utilize similar mechanisms for catalysis. Recently, bioinformatic analysis of the ACMSD enzyme family and biochemical characterization of *Pf*ACMSD revealed that ACMSD belongs to a large metal-dependent amidohydrolase superfamily (16). Several members of this superfamily are structurally and functionally well characterized (17–19). The members of this superfamily of enzymes contain either a mono- or dinuclear metal center embedded in a $(\beta/\alpha)_8$ barrel fold (18). The conserved metal ligands were predicted for ACMSD on the basis of multiple-sequence alignment analysis. Mutagenesis and spectroscopic analysis of these mutants further established their critical roles in metal binding and catalysis (16). These studies represent important progress in our understanding of ACMSD mechanisms and led to the realization that the metal-dependent nonoxidative decarboxylation catalyzed by ACMSD appears to be unique among all decarboxylases characterized so far (15, 16).

Here we report high-resolution crystal structure of native ACMSD from *P. fluorescens* as well as the structure of the cobalt-substituted enzyme. The identity of the native active site metal was determined to be Zn, and the catalytic efficiency of Zn-bound *Pf*ACMSD was shown to be comparable to that of the cobalt-reconstituted enzyme. As predicted, the structure of *Pf*ACMSD reveals a $(\beta/\alpha)_8$ barrel fold. The active site configuration of *Pf*ACMSD shares a significant degree of similarity with that of the Zn-dependent adenosine deaminase (ADA) and the Fe-dependent cytosine deaminase (CDA). Taken together, these data enable us to propose possible catalytic mechanisms of ACMSD which may serve as working hypotheses to guide future biochemical and mechanistic investigation of this important enzyme.

MATERIALS AND METHODS

Expression and Purification of Native *Pf*ACMSD. The cloning and expression of native *Pf*ACMSD have been described previously (4, 15). A different purification scheme was developed to produce pure *Pf*ACMSD for crystallization experiments. Briefly, the clarified cell lysate containing

overexpressed *Pf*ACMSD was first loaded onto a Q-Sepharose HP column (GE Healthcare Life Sciences, Piscataway, NJ) pre-equilibrated with 50 mM Hepes (pH 7.5) and 1 mM dithiothreitol (DTT). The bound proteins were eluted with a gradient of NaCl (from 0 to 1.0 M). Fractions containing *Pf*ACMSD were pooled, and a 3 M $(\text{NH}_4)_2\text{SO}_4$ stock solution was added dropwise to the *Pf*ACMSD pool to a final concentration of 1.25 M $(\text{NH}_4)_2\text{SO}_4$. The mixture was then loaded onto a Phenyl Sepharose column (GE Healthcare Life Sciences) pre-equilibrated with 50 mM Hepes (pH 7.5), 1.5 M $(\text{NH}_4)_2\text{SO}_4$, and 1 mM DTT and eluted with a linear gradient of $(\text{NH}_4)_2\text{SO}_4$ decreasing from 1.5 to 0.0 M. The fractions containing *Pf*ACMSD were more than 95% pure as judged by SDS–PAGE. They were pooled and dialyzed at 4 °C overnight against a buffer containing 50 mM Hepes (pH 7.5), 150 mM NaCl, and 1 mM DTT. The dialyzed sample was concentrated to a final concentration of 28 mg/mL for crystallization. The selenomethionyl *Pf*ACMSD was expressed in minimal medium supplemented with selenomethionine and other nutrients according to the established protocol (20) and purified by the same procedure as the native protein.

Crystallization and Data Collection. The initial crystal hit was obtained from the Wizard Sparse Matrix screening kit (Emerald Biostructures, Bainbridge Island, WA) using the hanging drop vapor diffusion method at 20 °C. This initial condition was optimized, and larger tetragonal and bipyramidal crystals were obtained. Under the final crystallization conditions, the reservoir solution contained 0.1 M Tris (pH 8.75), 15% PEG 5000, and 0.2 M MgCl_2 . An equal volume of protein and reservoir solution was mixed and equilibrated in the hanging drop vapor diffusion setting. The crystals typically appeared within 1 week. These crystals belong to space group $P4_22_12$ and diffract to ~ 2.8 Å resolution with the following unit cell dimensions: $a = b = 91.89$ Å and $c = 168.47$ Å. These crystals were not very stable and started deteriorating after ~ 2 weeks. In some of the drops, large plate crystals appeared after 3–4 weeks, which diffracted to much higher resolution (~ 1.65 Å). These plate crystals belong to space group $C2$ with the following unit cell dimensions: $a = 153.57$ Å, $b = 48.11$ Å, $c = 110.70$ Å, and $\beta = 127.31^\circ$. The tetragonal selenomethionyl *Pf*ACMSD crystals were obtained under conditions similar to those for the native protein. The crystals of *Pf*ACMSD grown in the presence of 5 mM CoCl_2 (Co–*Pf*ACMSD) were also obtained under similar conditions, and they belong to the same $P4_22_12$ space group as the native tetragonal crystals and diffract to 2.5 Å resolution.

All *Pf*ACMSD crystals were flash-frozen in liquid propane after being transferred stepwise to cryoprotectant solutions containing all the ingredients of the crystallization reservoir solution and 10%, 20%, and finally 30% PEG400. All data used in the structure determination was collected on beamline 19BM, Advanced Photon Source, Argonne National Laboratory, Argonne, IL (Table 1).

Phasing and Refinement. The initial phases of *Pf*ACMSD crystal were determined by the multiwavelength anomalous dispersion (MAD) phasing method using SOLVE 2.06 (21) with data collected from a selenomethionyl *Pf*ACMSD crystal at four wavelengths corresponding to the peak, the inflection point, a high-energy remote, and a low-energy remote point near the selenium K edge. Two *Pf*ACMSD

Table 1: Crystal Data and Refinement Statistics of *Pf*ACMSD

	SeMet				native	cobalt
	peak	inflection	high remote	low remote		
wavelength (Å)	0.97904	0.97918	0.97818	0.98034	0.97951	0.97945
resolution (outer shell) (Å)	30–2.8 (2.85–2.8)	30–2.8 (2.85–2.8)	30–2.8 (2.85–2.8)	30–2.8 (2.85–2.8)	30–1.65 (1.70–1.65)	30–2.5 (2.6–2.5)
total no. of observations	148978	148517	148131	149113	330133	199589
no. of unique observations	33974	33890	33594	33846	72711	25447
completeness (%) (outer shell)	99.8 (100.0)	99.8 (100.0)	99.8 (100.0)	99.7 (100.0)	93.0 (63.5)	99.4 (100)
R_{sym} (outer shell) ^a	0.053 (0.481)	0.054 (0.442)	0.053 (0.495)	0.049 (0.472)	0.032 (0.309)	0.062 (0.446)
I/σ (outer shell)	26.5 (3.8)	25.9 (3.2)	29.0 (4.5)	30.2 (4.2)	24.6 (2.6)	45.0 (5.3)
figure of merit	0.72					
Refinement						
R_{work}^b (%)					19.6	18.9
R_{free}^c (%)					24.0	23.8
no. of protein atoms					5190	5190
no. of waters					467	127
no. of ions					2 Zn, 1 Mg	2 Co
rmsd for bond lengths (Å)					0.016	0.012
rmsd for bond angles (deg)					1.58	1.35
Average B -factor (Å ²)						
protein atoms					43.2	66.5
water					49.7	61.2
ions					47.3	55.4
Ramachandran plot						
most favored region (%)					89.3	91.6
additionally allowed region (%)					9.8	8.2
generously allowed region (%)					0.5	0.2
disallowed region (%)					0.4	0.0

^a $R_{\text{sym}} = \sum_{hkl} [(\sum_j |I_j - \langle I \rangle|) / \sum_j |I_j|]$. ^b $R_{\text{work}} = \sum_{hkl} |F_o - F_c| / \sum_{hkl} |F_o|$, where F_o and F_c are the observed and calculated structure factors, respectively. ^c R_{free} is the value calculated for a randomly selected 5% of the reflections that were omitted from the refinement.

monomers were predicted to be in the asymmetric unit (ASU) of the tetragonal crystals, given a Matthews coefficient of 2.39 Å³/Da and a solvent content of 48%. Twenty-four of twenty-six Se sites from the two *Pf*ACMSD monomers were located. Density modification was performed using RESOLVE 2.06 (21), which resulted in a clearly interpretable electron density map with a final figure of merit of 0.72. The *Pf*ACMSD polypeptide chain was manually built into this map using O (22). This unrefined model was used as the initial search model for finding the positions of the *Pf*ACMSD molecules in the monoclinic unit cell of the native crystal. The molecular replacement method of Molrep (23) was used in the search. Two *Pf*ACMSD molecules were located in the asymmetric unit, and model refinement was carried out using CNS (24) with a simulated annealing protocol. The final rounds of refinement were performed with refmac5 (25) in the CCP4 package (26). The refined native *Pf*ACMSD model was then used as the starting model for the refinement of the Co-*Pf*ACMSD complex structure. The crystal data and refinement statistics are listed in Table 1.

Enzyme Activity Assay. The coupled enzyme activity assay on the recombinant *Pf*ACMSD in its native form was performed according to the procedures described previously (15, 16). The reaction mixture contained 0–40 μM ACMS and 0.1 μM ACMSD protein in 25 mM Hepes buffer (pH 7.0). The specific activity was calculated from the initial rates of ACMS decay monitored at 320 and 360 nm.

RESULTS AND DISCUSSION

Description of the *Pf*ACMSD Structure. As predicted from protein sequence analysis (16), the overall fold of ACMSD contains a distorted (β/α)₈ closed barrel and a small insertion

domain between strand β 1 and helix α 1 (Figure 1). This insertion domain is not found in other characterized amido-hydrolase structures and appears to be a unique feature of the ACMSD structure. It contains a short helix (α 1') and a small three-stranded β -sheet comprising strands β 1'– β 3'. As will be discussed later, this small insertion domain is thought to play a role in substrate binding. A short extension after the last helix, α 8, of the barrel contains two short helices (α 9 and α 10), which caps the bottom (N-terminal ends of the strands) of the barrel. A single metal ion coordinated by several protein residues is located at the opening of the barrel near the C-terminal ends of several β -strands. The detailed configuration of this metal center will be described in the next section.

There are two *Pf*ACMSD monomers (monomers A and B) in the asymmetric unit of the native crystals (Figure 2). Given the high resolution of the data (1.65 Å), both monomers are refined independently. The two monomers are very similar except in three surface regions: residues 17–46 (the unique insertion domain), 149–156 (loop between β 4 and α 4), and 178–187 (loop between β 5 and α 5). If these three regions are excluded, the average root-mean-square deviation (rmsd) in the C α positions of the two monomers is 0.41 Å. Notably, these three regions are largely disordered in monomer B as indicated by the high B -factors and poorly defined electron densities. The disordering of these regions may contribute to the relatively high R_{factor} and R_{free} for a structure refined at such resolution (Table 1). The dimer interface buries a surface area of ~2529 Å² on each monomer. The elution profile of *Pf*ACMSD from a size exclusion chromatography column indicates that the protein exists in solution as a mixture of both monomer and dimer forms (data not shown).

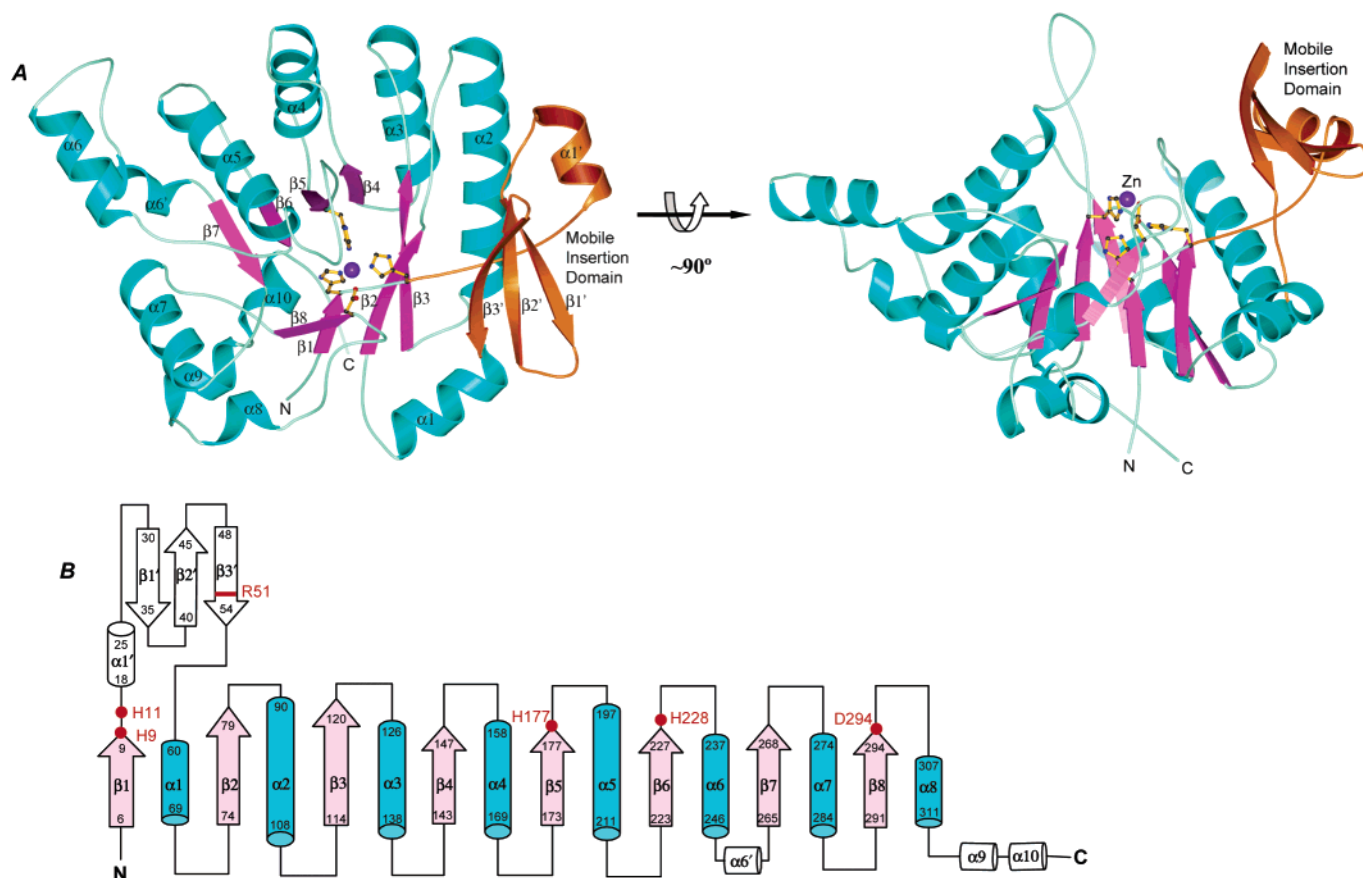


FIGURE 1: Ribbon diagram of the *PfACMSD* monomer (A) and topology diagram showing the *PfACMSD* fold (B). Two orthogonal views of *PfACMSD* are shown. The secondary structure elements of the $(\beta/\alpha)_8$ barrel core are labeled $\beta 1$ – $\beta 8$ for strands (colored magenta) and $\alpha 1$ – $\alpha 8$ for helices (colored cyan). The mobile insertion domain consists of $\alpha 1'$ and $\beta 1'$ – $\beta 3'$ (colored orange). The bound Zn ion is drawn as a purple sphere, while the protein residues ligated to Zn are shown in ball-and-stick representation. Amino acid numbers are indicated at the starting and ending points of the strands and helices in the topological representation. The positions of several important active site residues are also marked. This figure was generated using Molscript (39) and Gl_render (L. Esser, personal communication).

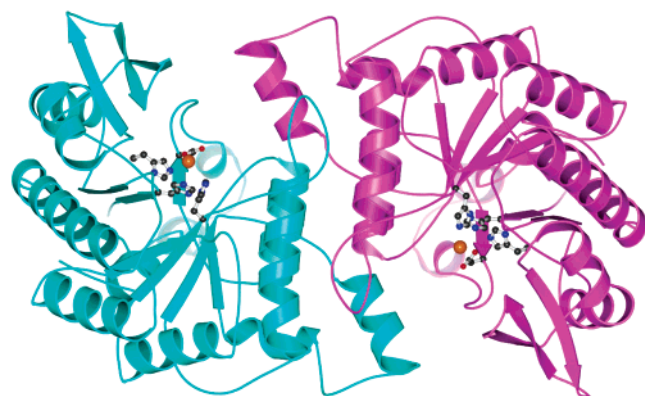


FIGURE 2: Ribbon diagram of the *PfACMSD* dimer. The two monomers are colored cyan and magenta, respectively. The bound metal ion and metal ligands are shown in ball-and-stick representation.

The search for similar structures in the Protein Data Bank (27) with DALI (28) found among its top hits several members in the “metal-dependent hydrolase” superfamily of the “TIM α/β -barrel fold” as classified in the SCOP database (29). These include isospartyl dipeptidase (PDB entry 1onw; Z-score = 15.6) (30), adenosine and cytosine deaminases (PDB entries 1a4m and 1k6w, respectively; Z-score = 14.5) (31, 32), phosphotriesterase (PDB entry 1psc; Z-score = 13.4) (33), and urease (PDB entry 1fwb; Z-score = 12.7) (34). The overall rmsd values of the superimposable C_α

positions (~ 220 residues out of 334 in *PfACMSD*) between *PfACMSD* and these structures range from 3.0 to 4.3 Å, and the levels of sequence identity range from 10 to 15%. From both the structure similarity and the sequence conservation pattern (16), ACMSD clearly belongs to this metal-dependent amidohydrolase superfamily and represents the only decarboxylase activity in this superfamily.

Active Site of Native *PfACMSD*. The clear electron density map of the *PfACMSD* structure revealed a single metal ion located near the C-termini of several β -strands of the $(\beta/\alpha)_8$ barrel core (Figure 3). To determine the identity of the metal ion, we performed an X-ray fluorescence scan on a native *PfACMSD* crystal at Advanced Photon Source synchrotron beamline 19BM. The result indicated that the endogenously bound metal ion was Zn (data not shown). The same experiment was also conducted on a Co-complexed *PfACMSD* crystal and confirmed the presence of Co in the crystal and the disappearance of the Zn fluorescence signal.

The Zn-containing native *PfACMSD* was initially found to be enzymatically inactive. Later, when the ammonium sulfate fraction was dropped from the original purification protocol, the as-isolated enzyme exhibited a specific activity of 800–1900 nmol min⁻¹ mg⁻¹ (numbers varied depending on sample preparations) under standard assay conditions described in Materials and Methods. In contrast, the Co-reconstituted enzyme exhibited an activity of 6000 nmol min⁻¹ mg⁻¹ under the same assay conditions (15). The

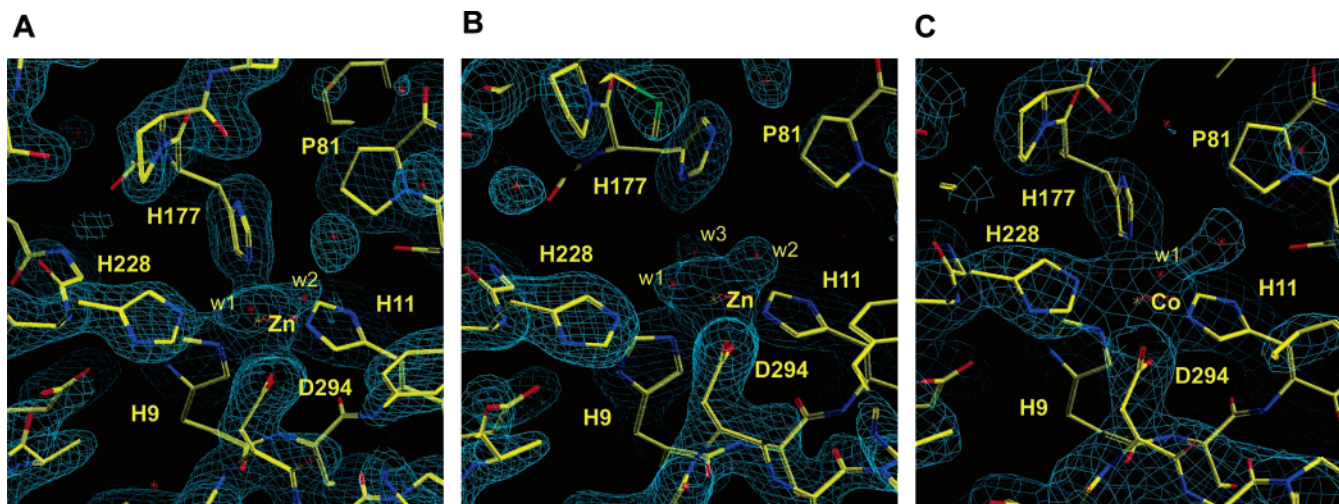


FIGURE 3: Electron density map ($2F_o - F_c$) at the active site metal center in (A) monomer A of the native *Pf*ACMSD dimer at 1.65 Å resolution, (B) monomer B of the native *Pf*ACMSD dimer, and (C) the Co-*Pf*ACMSD structure at 2.50 Å resolution. The maps are contoured at a 1.2σ level.

Table 2: Kinetic Properties of Zn- and Co-Containing ACMSD Enzymes

ACMSD metal ion	K_m (μ M ACMS)	k_{cat} (s^{-1})	k_{cat}/K_m ($\times 10^5 s^{-1} M^{-1}$)
Co(II)	23.2 ± 0.1	7.3 ± 0.1	3.1 ± 0.1
Zn(II)	9.6 ± 1.1	6.5 ± 1	6.9 ± 0.4

enzymatic activity of the as-isolated Zn-containing native enzyme was maximized to $4400 \text{ nmol min}^{-1} \text{ mg}^{-1}$ when the protein was incubated with ZnCl_2 for 3–5 h at 4 °C prior to the assay, making Zn the most active metal ion next to cobalt. The fact that the specific activity increased with added Zn suggests that the metal center was not fully occupied in the as-isolated protein. This is consistent with the observation that in the crystal structure, the *B*-factors for both Zn ions in the *Pf*ACMSD dimer are lower than those of the surrounding protein atoms (47 Å^2 vs 30 Å^2 in the A site and 58 Å^2 vs 42 Å^2 in the B site), indicating partial occupancy at both sites. The steady-state kinetic measurement of Zn- and Co-*Pf*ACMSD showed that the k_{cat} values for the two metals are quite comparable (Table 2), while the K_m of the Zn enzyme is less than half of that of the Co enzyme. As a result, the Zn-*Pf*ACMSD complex actually has a slightly higher catalytic efficiency (k_{cat}/K_m) than the Co enzyme. We found that ammonium sulfate indeed had an adverse effect on *Pf*ACMSD activity, with a stronger influence on the Zn form than on the Co enzyme (data not shown).

In monomer A of the native *Pf*ACMSD dimer, the Zn ion directly coordinates the side chains of His9, His11, His177, and Asp294 and an active site water molecule, w1 (Figure 4). A second water molecule, w2, may also ligate to the metal, although the distance between this water molecule and the metal ion is longer (2.43 Å) than that of a normal Zn ligand (Table 3). The *B*-factor for w2 is also higher than that for w1 (49 Å^2 vs 31 Å^2). Therefore, w2 is not as well ordered as w1 and may represent an alternative water ligand position with a much lower occupancy. Another invariant active site residue of the superfamily, His228 of *Pf*ACMSD, does not directly ligate to the Zn: the distance between NE2 of His228 and the Zn is 3.24 Å , too long for His228 to be a metal ligand. Instead, His228 is hydrogen-bonded to water ligand w1.

Interestingly, the configurations of the metal binding sites in the two monomers of the *Pf*ACMSD dimer are somewhat different (Figure 5). In monomer B, the active site Zn ion directly coordinates to His9, His11, Asp294, and three water molecules, all of which are within acceptable coordination distances (Table 3). Unexpectedly, the side chain of His177 in monomer B swings away and is no longer directly coordinated to the Zn. A third water molecule, w3, now replaces His177 as a metal ligand. Additionally, His228 moves farther from the metal (4.49 Å compared to 3.24 Å in monomer A). As a result, w1 in monomer B shifts its position compared to the corresponding water molecule in monomer A and remains hydrogen bonded to His228 (Figure 5). It should be noted that several regions surrounding the active site of monomer B exhibit significantly more conformational flexibility than the corresponding regions in monomer A. The *B*-factor of the bound Zn ion is also higher than that of Zn in monomer A (58 Å^2 vs 48 Å^2), indicating a lower occupancy or higher mobility.

Metal Center in the Co-*Pf*ACMSD Structure. Because cobalt was previously shown to be a highly potent metal ion for *Pf*ACMSD (15), we also determined the crystal structure of *Pf*ACMSD complexed with Co at 2.5 Å resolution. The substitution of Co for Zn in the protein was confirmed by an X-ray fluorescence scan. Although there are also two crystallographically independent monomers in the tetragonal Co-*Pf*ACMSD crystal, the overall conformations of the two monomers are very similar with an average rmsd for all C_α positions of 0.47 Å . Unlike the native enzyme structure, the configurations of the two active site metal centers in the Co-*Pf*ACMSD crystal are essentially the same given the resolution of the structure. Compared to the native enzyme, the overall structure of the Co-*Pf*ACMSD complex is particularly similar to monomer A of the native dimer, with a rmsd of 0.37 Å among all C_α atoms. Interestingly, the metal center of the Co-*Pf*ACMSD complex displays additional variations from those observed in the native enzyme (Figure 5). Besides His9, His11, His177, and Asp294 that directly coordinated to the metal, His228 now moves closer to the bound Co ion with a distance of 2.45 Å between NE2 and the metal (compared to 3.24 Å in the A site of the native enzyme) (Table 3). As a result, only one water ligand

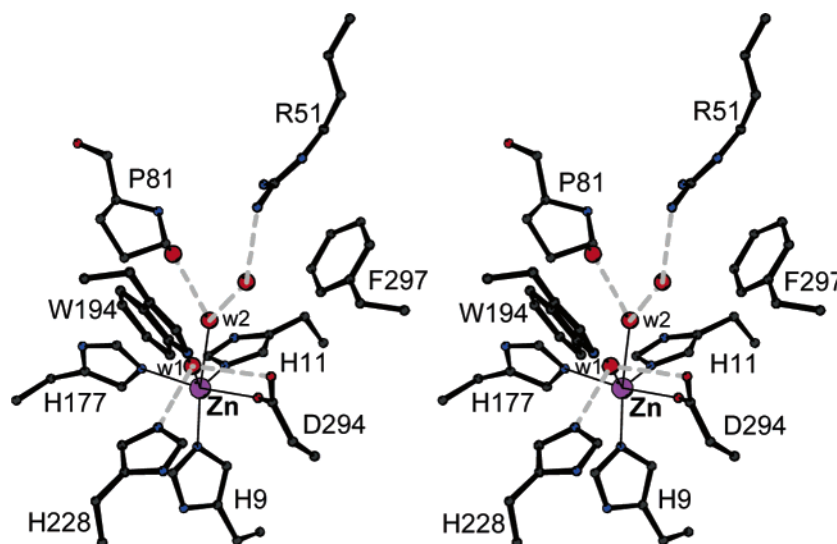


FIGURE 4: Stereoview of the active site metal center of monomer A in native *Pf*ACMSD. The Zn ion is shown as a purple sphere. The active site water molecules are shown as red spheres. Solid lines represent direct coordination to the metal, while dashed lines represent hydrogen bonds.

Table 3: Distances between the Active Site Metal and Metal Ligands in *Pf*ACMSD Crystals

component	site A (Å)	site B (Å)	interaction
native <i>Pf</i> ACMSD			
Zn–His228	3.24	4.49	H-bond/no interaction
His228–w1	2.50	2.71	H-bond
Zn–His9	2.17	2.18	ligand
Zn–His11	2.21	2.20	ligand
Zn–His177	2.10	4.25	ligand/nonligand
Zn–Asp294	2.16	2.14	ligand
Zn–w1	2.04	2.07	ligand
Zn–w2	2.43	2.29	ligand
Zn–w3	— ^a	2.28	ligand
Co– <i>Pf</i> ACMSD			
Co–His228	2.45	2.44	ligand
His228–w1	2.95	— ^b	H-bond
Co–His9	2.12	2.13	ligand
Co–His11	2.02	2.20	ligand
Co–His177	2.32	2.22	ligand
Co–Asp294	2.21	2.15	ligand
Co–w1	2.22	— ^b	ligand

^a Water w3 is not observed in the active site of monomer A in native *Pf*ACMSD. ^b The density for this water is not well defined in monomer B of the Co–*Pf*ACMSD complex.

can be located at the remaining coordination position of Co (Figure 5). This active site configuration is slightly different from the EPR results which point to a pentacoordinated metal cofactor with a distorted trigonal bipyramidal geometry determined in the frozen solution at a different pH, i.e., Hepes 7.0 (15). While the Tris-HCl buffer used for crystallization in this work had a pH of 8.75, Co-reconstituted *Pf*ACMSD was found to be most active at pH 6–7. The observation that His228 becomes a weak metal ligand in the Co–*Pf*ACMSD structure may explain some unusual low-temperature EPR properties as observed in the previous study (15). For instance, nitrogen and cobalt hyperfine coupling interactions can be observed at <6 K. However, mutational analysis of His228 has established that the major role of this residue is probably as an active site catalyst rather than a metal ligand (16).

The observation that His177 can dissociate from Zn in the crystal structure furnishes a rationale for the previous observation that the H177A mutant retained ca. 6% of the

wild-type enzyme activity while other metal ligand mutants preserved less than 0.5% of the activity (16). The optical and EPR properties of the H177A mutant were also more similar to those of the wild-type enzyme than those of the other mutants. Apparently, His177 is a more flexible ligand to the metal, which can transiently dissociate from the metal under certain conditions. Nevertheless, the crystal structures as well as previous mutational and spectroscopic analysis clearly showed that His177 contributed critically to the metal binding in *Pf*ACMSD. Both His177 and His228 side chains exhibit considerable conformational flexibility, which may correlate with the identity of the metal as well as the metal ion occupancy in the active site. The difference in the metal center configurations between the Zn– and Co–*Pf*ACMSD complexes may be responsible for their slightly different steady-state kinetic properties.

Putative Substrate-Binding Pocket. Inspection of the *Pf*ACMSD active site revealed a small pocket adjacent to the metal center that is lined with residues Trp194, Phe297, Pro81, and Arg51 (Figures 3 and 4). While Trp194 and Pro81 are uniquely conserved only in ACMSD protein sequences, Arg51 and Phe297 are also invariant residues in a closely related enzyme, isoorate decarboxylase (IDCase) (data not shown). Further biochemical experiments are required to establish the precise roles for these active site residues. There are several ordered water molecules in this pocket that are hydrogen-bonded to the metal-coordinating water molecule(s) and to the surrounding protein atoms. These solvent molecules presumably occupy part of the substrate-binding site. Of particular interest is residue Arg51, which resides on strand $\beta 3'$ of the mobile insertion domain and intrudes into the active site to interact with an active site water molecule (Figure 4). Replacement of this arginine with other amino acids in human and *P. fluorescens* enzymes resulted in a complete loss or significant reduction of the decarboxylase activity (A. Liu et al., unpublished data). The location of Arg51 suggests that this residue is most likely involved in the binding of substrate ACMS, presumably with one of its negatively charged carboxylate groups. The likely involvement of Arg51 in substrate binding suggests a role for the

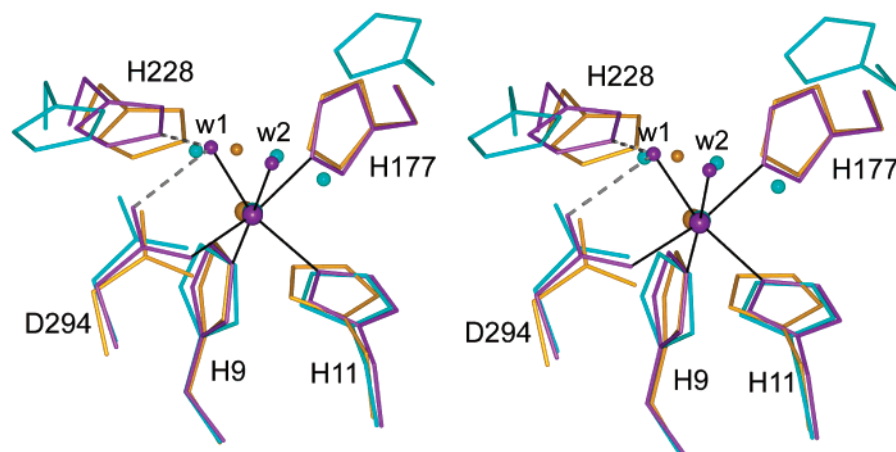


FIGURE 5: Stereoview of the superposition of the metal centers in monomers A and B of the native *Pf*ACMSD dimer (colored purple and cyan, respectively), as well as in the Co-*Pf*ACMSD complex (colored yellow). The metal coordination and hydrogen bonds in the A site of native *Pf*ACMSD are represented by solid and dashed lines, respectively.

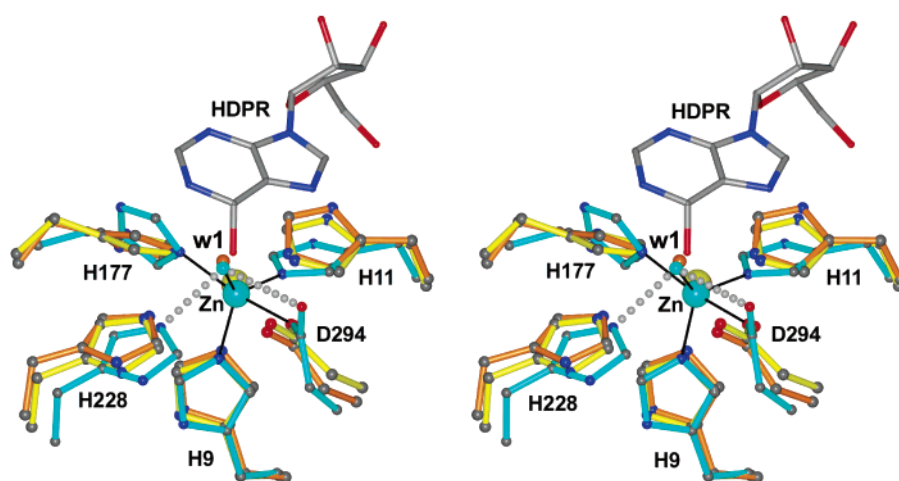


FIGURE 6: Stereoview of the metal center in native *Pf*ACMSD (cyan) superimposed with that in adenosine deaminase (ADA, yellow) (31) and cytosine deaminase (CDA, orange) (32). The metal coordination and hydrogen bonds in *Pf*ACMSD are indicated by solid and dotted lines, respectively. The bound inhibitor or transition-state analogue of ADA (HDPR, 6-hydroxy-1,6-dihydropurine ribonucleoside) (36) is also shown.

mobile insertion domain in ACMSD function. This mobile domain probably undergoes conformational changes upon substrate binding and switches between an “open” and a “closed” conformation corresponding to the substrate-free and substrate-bound states of the enzyme, respectively. In the substrate-bound state, this domain would provide additional active site residues such as Arg51 and shield the active site from the surrounding solvent.

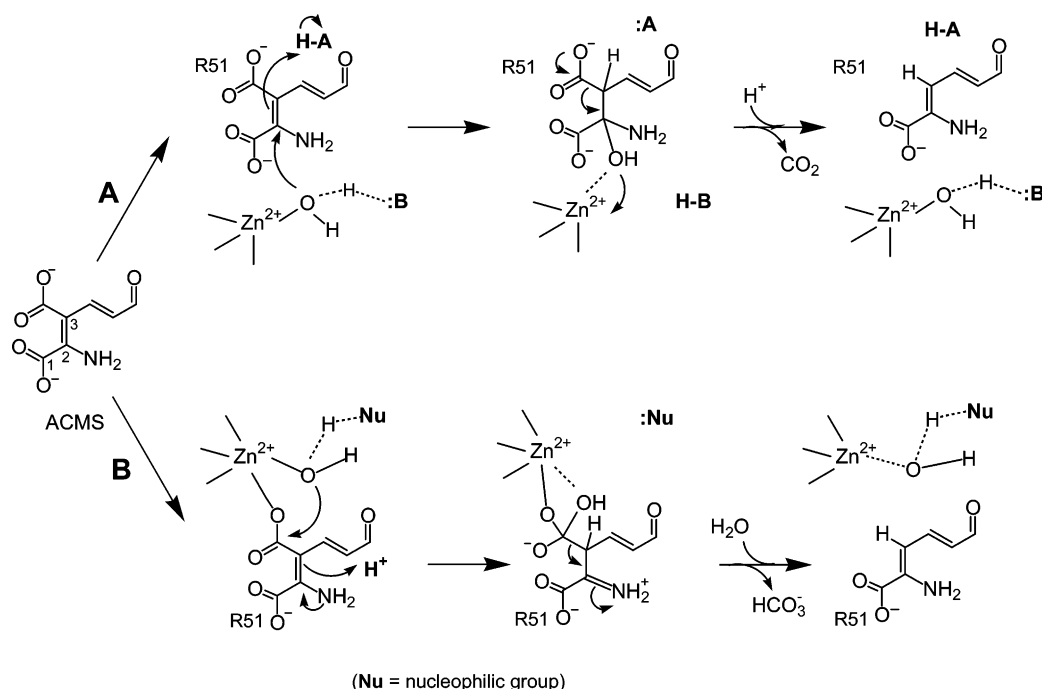
Comparison of ACMSD with Other Members of the Amidohydrolase Superfamily. The structure solution of *Pf*ACMSD and the observed active site configurations validated our previous predictions (16), in particular, the TIM barrel fold for the overall protein architecture and the assignment of ACMSD to the amidohydrolase superfamily. The diverse amidohydrolase superfamily currently contains more than 2000 protein sequences as presented in the Pfam database [accession numbers PF01979 and PF04909 (35)] and includes ~17 characterized unique activities. Because a decarboxylation reaction that cleaves a C–C bond is unprecedented in this superfamily, ACMSD thus represents an important addition that further enhances the functional diversity of this large group of homologous proteins.

Comparison of the ACMSD active site with those structurally characterized proteins in the amidohydrolase superfamily

reveals that the metal center configuration of ACMSD closely resembles the subtype III metal center of the superfamily (17). This type of mononuclear metal center is found in adenosine deaminase (ADA) and cytosine deaminase (CDA) (31, 32, 36). A superposition of active site A of native *Pf*ACMSD with those of ADA and CDA is presented in Figure 6. All five metal ligands, His9, His11, His177, Asp294, and the water ligand (w1 in *Pf*ACMSD), as well as the conserved nonmetal ligand histidine residue (His228 in *Pf*ACMSD) superimpose very well among the three structures. The striking similarity between the metal center configurations in these enzymes suggests that they may share some common aspects in their catalytic mechanism, which should help in developing a working hypothesis that may lead to the unraveling of the mechanism of ACMSD.

Proposed Catalytic Mechanism. The key aspects of the chemistry employed by ADA, CDA, and other enzymes of the amidohydrolase superfamily are the addition of a metal-bound hydroxyl group to a substrate carbon atom to give a tetrahedral intermediate (17). It is likely that ACMSD also utilizes similar chemistry in its catalytic mechanism. In considering the potential mechanisms for ACMSD, one must take into account that the substrate ACMS bears two carboxyl groups, including the leaving carboxylate group at C3 and

Scheme 2: Proposed Mechanisms for ACMSD



the C2 carboxylate adjacent to an amino group (Scheme 2). At present, a complex structure of ACMSD with a substrate or substrate analogue is not yet available. The existence of several isomeric forms of ACMS in solution (5) and the flexibility of the active site conformation preclude reliable docking of the substrate into the active site of the enzyme by computer modeling. Nevertheless, two possible substrate binding modes can be envisioned in which either carboxylate group may be placed next to the metal center while the second carboxylate would interact with the side chain of Arg51. Thus, two drastically different potential mechanisms for ACMSD are proposed, and they are depicted in Scheme 2.

In the first mechanism (Scheme 2, route A), the C2 carboxylate binds next to the metal center and the metal-bound hydroxyl group functions as a nucleophile to attack at C2. The subsequent protonation of C3 gives a C3 tetrahedral intermediate that would promote an electron flow from C3 carboxylate to C2 and lead to the final decarboxylation. In this mechanism, the candidate protein residues that may function as the general base to help generate the catalytic hydroxyl are Asp294 and His228, both of which are hydrogen-bonded with w1 in the crystal structure (Figure 4). The candidate for the general acid in the scheme that is required to protonate C3 is either His228 or His177 because of the proximity of each to the substrate. In this mechanism, Arg51 would interact with the C3 carboxylate of the substrate and help to orient it in the active site, but it needs to be dissociated from the reaction intermediate for the CO₂ product to be released. The conformational flexibility of the mobile insertion domain where Arg51 resides may provide a mechanism for this requirement of Arg51 function.

In the second mechanism (Scheme 2, route B), the C3 leaving carboxylate binds next to the Zn with one of its oxygens directly ligated to the metal. The water ligand (w1) is activated by an active site base to become a more nucleophilic hydroxide ion, which attacks the carbon atom

of the leaving carboxylate group. With the concomitant protonation of C3, a tetrahedral intermediate different from that in route A is generated. The HCO₃⁻ group of the intermediate is stabilized by the direct coordination to the Zn ion in a manner similar to that found in carbonic anhydrases (37, 38). The subsequent exchange of zinc-bound HCO₃⁻ with a water molecule facilitates the dissociation of the product and restores the water ligand. In this route, Arg51 would interact with the C2 carboxylate group and position the substrate correctly in the active site. One concern for the mechanism presented in route B is that it might be energetically unfavorable for a negatively charged hydroxyl group to attack a negatively charged carboxylate group. Presumably, interactions of the substrate with the surrounding protein residues and in particular the interactions with the metal ion will help to overcome this energy barrier. The direct ligation of the C3 carboxylate of the substrate to the metal ion will be a prerequisite for this mechanism to be valid.

There are several important differences in the two proposed mechanisms. First, the substrate binds to the active site pocket in opposite orientations. The determination of the crystal structure of the enzyme complexed with the substrate or substrate analogues will be required to distinguish the exact binding mode of the substrate. Second, the conformations of the tetrahedral transition-state intermediates are different. Third, the final products from the two mechanisms are also different. While the product from route A is CO₂, it is HCO₃⁻ from route B. It should be pointed out that only the key steps of the two proposed mechanisms are outlined in Scheme 2. There are more detailed chemical processes involved in each mechanism that are not possible to address at the moment. For example, it is not clear whether the hydroxyl group addition and C3 protonation occur sequentially or simultaneously. The exact roles for the active site protein residues also need to be further investigated so that the putative acid–base catalysts can be identified unambigu-

ously. Clearly, trapping the substrate- and inhibitor-bound enzyme intermediates and characterizing their structures will be most informative with regard to the mechanism of the enzyme and is apparently the next critical step toward a better understanding of ACMSD mechanism. Extensive mutational and kinetic characterizations of the active site residues are also required to understand the precise roles of the proposed active site residues.

In summary, the high-resolution crystal structures of *Pf*ACMSD reveal a detailed atomic arrangement of the active site metal center and identify additional active site residues such as Arg51 and His228 as well as a putative substrate-binding pocket. Significant conformational flexibilities are observed for active site residues His228 and His177 in the crystal structures. The implication of such conformational flexibility in substrate binding and catalysis remains to be illustrated. The active site conformation of ACMSD is shown to be very similar to that of adenosine deaminase and cytosine deaminase, whose structures and mechanisms are well understood. We have proposed two possible mechanisms for the ACMSD-catalyzed decarboxylation reaction that can be experimentally tested. Further structural and biochemical studies are currently underway aimed at unraveling the unusual mechanism of this important enzyme.

ACKNOWLEDGMENT

We thank Professor Yoshie Hasegawa for providing us with the *Pf*ACMSD overexpression system, Nick Grishin for stimulating discussions and critical reading of the manuscript, and Diana Tomchick for helping with synchrotron data collection. We are grateful to Professors Tadhg P. Begley, Robert P. Hausinger, Frank M. Raushel, and Hung-wen Liu for constructive discussions about enzyme mechanisms and their encouragement.

REFERENCES

- Kurnasov, O., Goral, V., Colabroy, K., Gerdes, S., Anantha, S., Osterman, A., and Begley, T. P. (2003) NAD biosynthesis: Identification of the tryptophan to quinolinate pathway in bacteria, *Chem. Biol.* 10, 1195–204.
- Magni, G., Amici, A., Emanuelli, M., Raffaelli, N., and Ruggieri, S. (1999) Enzymology of NAD⁺ synthesis, *Adv. Enzymol. Relat. Areas Mol. Biol.* 73, 135–82.
- Hasegawa, Y., Muraki, T., Tokuyama, T., Iwaki, H., Tatsuno, M., and Lau, P. C. (2000) A novel degradative pathway of 2-nitrobenzoate via 3-hydroxyanthranilate in *Pseudomonas fluorescens* strain KU-7, *FEMS Microbiol. Lett.* 190, 185–90.
- Muraki, T., Taki, M., Hasegawa, Y., Iwaki, H., and Lau, P. C. (2003) Prokaryotic homologs of the eukaryotic 3-hydroxyanthranilate 3,4-dioxygenase and 2-amino-3-carboxymuconate-6-semialdehyde decarboxylase in the 2-nitrobenzoate degradation pathway of *Pseudomonas fluorescens* strain KU-7, *Appl. Environ. Microbiol.* 69, 1564–72.
- Colabroy, K. L., and Begley, T. P. (2005) The pyridine ring of NAD is formed by a nonenzymatic pericyclic reaction, *J. Am. Chem. Soc.* 127, 840–1.
- Nishizuka, Y., Ichiyama, A., and Hayaishi, O. (1970) Metabolism of the benzene ring of tryptophan (mammals). II. Picolinic carboxylase (cat liver) (α -amino- β -carboxymuconic- ϵ -semialdehyde β -decarboxylase), *Methods Enzymol.* 17, 471–6.
- Wilson, R., and Henderson, L. (1962) Tryptophan-niacin relationship in *Xanthomonas pruni*, *J. Bacteriol.* 85, 221–8.
- Ichiyama, A., Nakamura, S., Kawai, H., Honjo, T., Nishizuka, Y., Hayaishi, O., and Senoh, S. (1965) Metabolism of the benzene ring of tryptophan in mammalian tissues. II. Enzymic formation of α -aminomuconic acid from 3-hydroxyanthranilic acid, *J. Biol. Chem.* 240, 740–9.
- Stone, T. W., and Darlington, L. G. (2002) Endogenous kynurenines as targets for drug discovery and development, *Nat. Rev. Drug Discovery* 1, 609–20.
- Schwarcz, R. (2004) The kynurenine pathway of tryptophan degradation as a drug target, *Curr. Opin. Pharmacol.* 4, 12–7.
- Schwarcz, R., Whetsell, W. O., Jr., and Mangano, R. M. (1983) Quinolinic acid: An endogenous metabolite that produces axon-sparing lesions in rat brain, *Science* 219, 316–8.
- Stone, T. W., Mackay, G. M., Forrest, C. M., Clark, C. J., and Darlington, L. G. (2003) Tryptophan metabolites and brain disorders, *Clin. Chem. Lab. Med.* 41, 852–9.
- May, E. L., and Mehler, A. H. (1956) Studies with carboxyl-labeled 3-hydroxyanthranilic and picolinic acids *in vivo* and *in vitro*, *J. Biol. Chem.* 223, 449–55.
- Mehler, A. H. (1956) Formation of picolinic and quinolinic acids following enzymatic oxidation of 3-hydroxyanthranilic acid, *J. Biol. Chem.* 218, 241–54.
- Li, T., Walker, A. L., Iwaki, H., Hasegawa, Y., and Liu, A. (2005) Kinetic and spectroscopic characterization of ACMSD from *Pseudomonas fluorescens* reveals a pentacoordinate mononuclear metallocofactor, *J. Am. Chem. Soc.* 127, 12282–90.
- Li, T., Iwaki, H., Fu, R., Hasegawa, Y., Zhang, H., and Liu, A. (2006) α -Amino- β -carboxymuconic- ϵ -semialdehyde decarboxylase (ACMSD) is a new member of the amidohydrolase superfamily, *Biochemistry* 45, 6628–34.
- Seibert, C. M., and Raushel, F. M. (2005) Structural and catalytic diversity within the amidohydrolase superfamily, *Biochemistry* 44, 6383–91.
- Holm, L., and Sander, C. (1997) An evolutionary treasure: Unification of a broad set of amidohydrolases related to urease, *Proteins* 28, 72–82.
- Gerlt, J. A., and Babbitt, P. C. (2001) Divergent evolution of enzymatic function: Mechanistically diverse superfamilies and functionally distinct suprafamilies, *Annu. Rev. Biochem.* 70, 209–46.
- Doublie, S. (1997) Preparation of selenomethionyl proteins for phase determination, *Methods Enzymol.* 276, 523–30.
- Terwilliger, T. C. (2002) Automated structure solution, density modification and model building, *Acta Crystallogr. D* 58, 1937–40.
- Jones, T. A., Zou, J.-Y., Cowan, S. W., and Kjeldgaard, M. (1991) Improved methods for building protein models in electron density maps and the location of errors in these models, *Acta Crystallogr. A* 47, 110–9.
- Vagin, A., and Teplyakov, A. (2000) An approach to multi-copy search in molecular replacement, *Acta Crystallogr. D* 56, 1622–4.
- Brünger, A. T., Adams, P. D., Clore, G. M., DeLano, W. L., Gros, P., Grosse-Kunstleve, R. W., Jiang, J. S., Kuszewski, J., Nilges, M., Pannu, N. S., Read, R. J., Rice, L. M., Simonson, T., and Warren, G. L. (1998) Crystallography & NMR system: A new software suite for macromolecular structure determination, *Acta Crystallogr. D* 54, 905–21.
- Murshudov, G. N., Vagin, A. A., and Dodson, E. J. (1997) Refinement of macromolecular structures by the maximum-likelihood method, *Acta Crystallogr. D* 53, 240–55.
- Collaborative Computational Project, Number 4 (1994) The CCP4 Suite: Programs for protein crystallography, *Acta Crystallogr. D* 50, 760–3.
- Berman, H. M., Westbrook, J., Feng, Z., Gilliland, G., Bhat, T. N., Weissig, H., Shindyalov, I. N., and Bourne, P. E. (2000) The protein data bank, *Nucleic Acids Res.* 28, 235–42.
- Holm, L., and Sander, C. (1995) Dali: A network tool for protein structure comparison, *Trends Biochem. Sci.* 20, 478–80.
- Murzin, A. G., Brenner, S. E., Hubbard, T., and Chothia, C. (1995) SCOP: A structural classification of proteins database for the investigation of sequences and structures, *J. Mol. Biol.* 247, 536–40.
- Thoden, J. B., Marti-Arbona, R., Raushel, F. M., and Holden, H. M. (2003) High-resolution X-ray structure of isoaspartyl dipeptidase from *Escherichia coli*, *Biochemistry* 42, 4874–82.
- Wang, Z., and Quiocho, F. A. (1998) Complexes of adenosine deaminase with two potent inhibitors: X-ray structures in four independent molecules at pH of maximum activity, *Biochemistry* 37, 8314–24.
- Ireton, G. C., McDermott, G., Black, M. E., and Stoddard, B. L. (2002) The structure of *Escherichia coli* cytosine deaminase, *J. Mol. Biol.* 315, 687–97.
- Benning, M. M., Kuo, J. M., Raushel, F. M., and Holden, H. M. (1995) Three-dimensional structure of the binuclear metal center of phosphotriesterase, *Biochemistry* 34, 7973–8.

34. Pearson, M. A., Michel, L. O., Hausinger, R. P., and Karplus, P. A. (1997) Structures of Cys319 variants and acetohydroxamate-inhibited *Klebsiella aerogenes* urease, *Biochemistry* 36, 8164–72.
35. Bateman, A., Coin, L., Durbin, R., Finn, R. D., Hollich, V., Griffiths-Jones, S., Khanna, A., Marshall, M., Moxon, S., Sonnhammer, E. L., Studholme, D. J., Yeats, C., and Eddy, S. R. (2004) The Pfam protein families database, *Nucleic Acids Res.* 32, D138–41.
36. Wilson, D. K., Rudolph, F. B., and Quioco, F. A. (1991) Atomic structure of adenosine deaminase complexed with a transition-state analog: Understanding catalysis and immunodeficiency mutations, *Science* 252, 1278–84.
37. Iverson, T. M., Alber, B. E., Kisker, C., Ferry, J. G., and Rees, D. C. (2000) A closer look at the active site of γ -class carbonic anhydrases: High-resolution crystallographic studies of the carbonic anhydrase from *Methanosarcina thermophila*, *Biochemistry* 39, 9222–31.
38. Christianson, D. W., and Fierke, C. A. (1996) Carbonic Anhydrase: Evolution of the Zinc Binding Site by Nature and by Design, *Acc. Chem. Res.* 29, 331–9.
39. Kraulis, P. J. (1991) MOLSCRIPT: A program to produce both detailed and schematic plots of protein structures, *J. Appl. Crystallogr.* 24, 946–50.

BI060903Q